Morphologic effects of nano CeO_2–TiO_2 on the performance of Au/CeO_2–TiO_2 catalysts in low-temperature CO oxidation

Shuna Li [a,b], Huaqing Zhu [a,*], Zhangfeng Qin [a,*], Guofu Wang [a], Yagang Zhang [a,b], Zhiwei Wu [a], Zhikai Li [a,b], Gang Chen [a,b], Weiwen Dong [a,b], Zhonghua Wu [c], Lirong Zheng [c], Jing Zhang [c], Tiandou Hu [c], Jianguo Wang [a,*]

[a] State Key Laboratory of Coal Conversion, Institute of Coal Chemistry, Chinese Academy of Sciences, P.O. Box 165, Taiyuan, Shanxi 030001, PR China
[b] University of Chinese Academy of Sciences, Beijing 100049, PR China
[c] Institute of High Energy Physics, The Chinese Academy of Sciences, Beijing 100049, PR China

ABSTRACT

CeO_2–TiO_2 composite nanorods and nanoparticles were synthesized by hydrothermal and co-precipitation methods, respectively; with the CeO_2–TiO_2 composite of different morphologies as supports, Au/CeO_2–TiO_2 catalysts were prepared by the colloidal deposition method and used in CO oxidation at ambient temperature. N_2 sorption, XRD, HRTEM, H_2-TPR, XPS and XAS characterizations were used to clarify the relationship between the morphologic properties of CeO_2–TiO_2 and the catalytic performance of Au/CeO_2–TiO_2. HRTEM results show that Au/CeO_2–TiO_2 nanorods are dominated by CeO_2 nanocrystals with (1 1 0) and (1 0 0) facets, while the Au/CeO_2–TiO_2 nanoparticles mainly expose (1 1 1) planes. XPS and XAS results reveal that both Au/CeO_2–TiO_2 nanorods and Au/CeO_2–TiO_2 nanoparticles are similar in the state of gold species. H_2-TPR results indicate that the presence of Au strongly promotes the reduction of CeO_2 in the Au/CeO_2–TiO_2 nanorods. The catalytic activity of Au/CeO_2–TiO_2 in CO oxidation is strongly related to the morphology of CeO_2–TiO_2; the CeO_2–TiO_2 nanorods as support endow the Au/CeO_2–TiO_2 catalyst with much higher activity than the CeO_2–TiO_2 nanoparticles. The (1 1 0) and (1 0 0) facets of CeO_2 dominated in the Au/CeO_2–TiO_2 nanorods are able to promote the oxygen migration and gold dispersion, which may then evidently enhance the redox capacity and catalytic activity of the Au/CeO_2–TiO_2 nanorods in CO oxidation at low temperature.

© 2013 Elsevier B.V. All rights reserved.

1. Introduction

The catalytic oxidation of CO at low temperature has attracted considerable attentions because of its wide applications in the exhaust abatement of carbon dioxide lasers, automotive emission control, trace CO removal in enclosed atmospheres, CO preferential oxidation for proton exchange membrane fuel cells, etc. Among various heterogeneous catalysts involved, supported noble metals, e.g. Au [1–5], Pd [6,7], and Pt [8–10], have been proved catalytically effective for CO oxidation. During the past two decades, intensive attention has been especially paid to gold catalysts due to their unique activity at low temperature.

Gold had been considered to be stable and catalytically inert until Haruta et al. discovered that small gold nanoparticles finely dispersed on certain metal oxide supports exhibit surprisingly high catalytic activity in low temperature CO oxidation [1,2,11]. They revealed that the size of the gold particles is crucial to the activity of gold catalysts. Meanwhile, it was also found that the catalytic properties of gold catalysts are also markedly influenced by the nature of support materials [2,12,13]. Among various supports, the reducible oxides such as TiO_2, Fe_2O_3, CeO_2 and Co_3O_4 are considered most active because of their excellent ability to provide reactive oxygen to the active gold sites [14]; the activity of supported gold catalysts is strongly related to many factors like the gold-support interface, support geometry and quantum size effects. More recently, it was reported that the morphology/shape of nano-scale supports also exhibits significant effect on the performance of gold catalysts. For examples, the activity of Au/CeO_2 catalysts in water–gas shift was affected by the shape of nanoscale ceria support [15] and the performance of gold catalysts in CO oxidation was strongly dependent on the morphology of α-Fe_2O_3 supports [16,17]. Han et al. found that the gold nanoparticles supported on γ-Al_2O_3 nanofibers were much more active than those supported on commercial γ-Al_2O_3 in CO oxidation [18].

Ceria was regarded as one of the most important components in many catalysts owing to its remarkable redox properties [19,20]. As a promoter in the three-way catalysts, ceria was able to improve

the noble metal dispersion and the thermal stability of alumina support as well as the ability of oxygen storage and release, which can then enhance their catalytic performance in CO oxidation and water–gas shift reactions [21,22]. The redox behavior of ceria can be modified by incorporation of other elements and the formation of mixed oxides. Ilieva et al. [23] investigated the preferential oxidation (PROX) of CO over gold catalysts supported on ceria doped with FeO_x, MnO_x and CoO_x prepared by co-precipitation (CP) and mechanochemical activation (MA) methods. The selection of dopants and preparation methods exhibited evident effects on the structure and properties of the resultant supports and catalysts; the gold catalysts supported on ceria prepared by MA and modified with FeO_x and MnO_x performed excellently in CO PROX with high activity and selectivity. Furthermore, gold nanoparticles dispersed on other ceria supports with various dopants, such as CeO_2–Al_2O_3 [24], CuO–CeO_2 [25], CeO_{1-x}–ZrO_x [26], CeO_2–Co_3O_4 [27] and CeO_2–TiO_2 [28] have also been found highly active in numerous reactions. Especially, as reported by Luo et al., the incorporation of titanium into ceria could significantly improve its mobile oxygen storage capacity [28]. In this respect, Ce–Ti–O mixed oxide has been investigated widely and the catalysts with Ce–Ti–O as support have been used in various reactions such as the oxidation of volatile organic compounds (VOCs) [29], partial oxidation of methane [30], steam reforming of ethanol [31] and low temperature CO oxidation [6,32–35]. In our previous works, Pd supported on CeO_2–TiO_2 mixed oxide exhibited high activity in CO oxidation at low temperature [6,32–34]. CuO supported on $Ce_{0.8}Ti_{0.2}O_2$ composite displayed high activity for CO PROX in H_2-rich stream [35]. However, to the best of our knowledge, the synthesis of CeO_2–TiO_2 composite oxide with different shapes in nanoscale and the morphologic effects of nanoscale CeO_2–TiO_2 support on the performance of Au/CeO_2–TiO_2 catalyst were scarcely reported.

The present work therefore focuses on the morphologic effects of nano CeO_2–TiO_2 on the performance of Au/CeO_2–TiO_2 catalyst in low-temperature CO oxidation. CeO_2–TiO_2 composite nanorods and nanoparticles were synthesized by hydrothermal and co-precipitation methods, respectively; with the CeO_2–TiO_2 composite of different morphologies as supports, Au/CeO_2–TiO_2 catalysts were prepared by the colloidal deposition method with the aim to exclude the influence of gold species on their catalytic behavior and to get deep insight into the effect of support morphology on the performance of Au/CeO_2–TiO_2 catalysts.

2. Experimental

2.1. Catalyst preparation

CeO_2–TiO_2 nanorods (a CeO_2/TiO_2 molar ratio of 8 was designated) were prepared by a modified hydrothermal method following the reported procedures [15]. Typically, $Ce(NO_3)_3 \cdot 6H_2O$ (4.0 mmol) and $Ti(SO_4)_2$ (0.5 mmol) were dissolved in aqueous KOH solution (90 ml, 6 M) in a Teflon beaker; the mixture was stirred continuously for 30 min at room temperature and then transferred into a Teflon-lined stainless steel autoclave, sealed and maintained at 110 °C for 24 h. After cooling down to the room temperature, the obtained solid product was recovered by filtration and washed with deionized water. The final solid product was dried at 80 °C for 12 h and calcined at 400 °C in air for 4 h. Contrastively, CeO_2–TiO_2 nanoparticles were prepared by the traditional co-precipitation method at 45 °C with $Ce(NO_3)_3 \cdot 6H_2O$ (44.4 mmol) and $Ti(SO_4)_2$ (5.6 mmol) as precursors and KOH solution (6 M) as precipitant. After aging and washing, the obtained products were dried at 80 °C for 12 h and calcined in air at 400 °C for 4 h. For the sake of convenience, the CeO_2–TiO_2 nanorods and CeO_2–TiO_2 nanoparticles obtained in this work are denoted as CeO_2–TiO_2-R and CeO_2–TiO_2-P, respectively.

Au supported catalysts were prepared through the colloidal deposition method as described by Comotti et al. [12,16]. Typically, polyvinyl alcohol (PVA) as protecting agent was added (Au/PVA ratio was 1.5 by weight) into aqueous gold solution (100 mg/L, as $HAuCl_4$) at room temperature under vigorous stirring. The obtained solution was then stirred further for 10 min. A given quantity of aqueous $NaBH_4$ solution (0.1 M; the molar ratio of $NaBH_4$/Au was 5) was then injected rapidly, which led to the formation of colloidal gold solution in dark orange-brown color. After that, the CeO_2–TiO_2 support was then added into the colloidal gold solution under stirring; the mixture was stirred until the solution was decolorized, which indicated a complete adsorption of Au on the support (gold loading of 1 wt.% was designated). In these previous steps, all the containers were covered with aluminum foil to exclude possible light irradiation. The resultant solid materials, i.e. the Au/CeO_2–TiO_2 catalysts, were collected by filtration and washed with deionized water. Finally, the Au/CeO_2–TiO_2 catalysts were then dried at 80 °C for 4 h and calcined at 250 °C in air for 4 h, unless otherwise specified.

2.2. Catalyst characterization

Brunauer–Emmett–Teller (BET) surface area of the catalysts was measured by nitrogen sorption at −195.8 °C with a TriStar 3000 Gas Absorption Analyzer (Micromeritics Instrument Co., USA). The samples were degassed at 200 °C and 6.7 Pa for 2 h prior to the measurement.

The actual composition of the catalysts was determined by inductively coupled plasma atomic emission spectroscopy (ICP-AES). To prepare the solution for elemental analysis, 2 ml of concentrated nitric acid was used to dissolve 40 mg of catalyst sample, followed by adding 2 ml of 30 wt.% H_2O_2; the solution was then diluted to 1000 ml with de-ionized water.

X-ray powder diffraction (XRD) patterns of the catalysts were collected on an advanced X-ray diffractometer (Bruker AXS D8, Germany) with monochromated Cu Kα radiation (154.06 pm, 40 kV, and 40 mA). The measurements were made at room temperature in the 2θ range of 5–85° with a scanning rate of 4°/min. The average crystallite size was estimated from the line broadening of the most intense XRD reflections with Scherrer formula and the cell parameter of cubic CeO_2 is obtained by the MDI Jade5 software.

Transmission electron microscopy (TEM) and high-resolution transmission electron microscopy (HRTEM) images of the catalyst samples were obtained by using a JEM 2010 microscope operating at 200 kV and equipped with an energy-dispersive X-ray (EDX) instrument. To get an appropriate electron transparence, the catalyst was crushed into fine powder and then a holey carbon film copper grid was dipped into the crushed powder.

Thermogravimetric (TG) analysis was conducted on a thermogravimetric analyzer of Setsys Evolution TGA 16/18 in an air flow from ambient temperature to 800 °C with a heating rate of 10 °C/min.

Temperature programmed reduction by hydrogen (H_2-TPR) was performed on a Micromeritics AutoChem II 2920 Chemisorption Analyzer. Approximately 100 mg of the catalyst sample (40–60 mesh) was used in each measurement [6,35]. The catalyst sample was first pretreated under an argon flow containing 5 vol.% oxygen (30 ml/min) at 250 °C for 30 min, followed by purging with pure argon (30 ml/min) at the same temperature for 30 min and then cooling down to 0 °C for the CeO_2–TiO_2 supports and to −10 °C for the Au/CeO_2–TiO_2 catalysts. After that, a flow of 10% hydrogen diluted in argon (30 ml/min) was switched into the system and the catalyst sample was heated up to 800 °C at a ramp of 10 °C/min. The amount of hydrogen uptake during the heating for reduction was measured by a thermal conductivity detector (TCD), which was

calibrated by quantitative reduction of a given quantity of CuO to metallic copper.

X-ray photoelectron spectroscopy (XPS) was performed on a ULVAC PHI-5800 spectrometer with Al Kα radiation and a multi-channel detector. Approximately 100 mg of the sample powder was compressed into a wafer for analysis. The survey spectra were measured in the binding energy (BE) range of 0–1100 eV; the detailed spectra of the Au 4f, Ce 3d and O 1s regions were measured in the ranges of 80–90 eV, 875–925 eV, and 520–540 eV, respectively. The BE values were calibrated with the signal of contaminated carbon C 1s at 284.6 eV. The spectra were decomposed by using XPSPEAK software (Ver. 4.1) after applying a Shirley background subtraction and Gaussian (80%)–Lorentzian (20%) decomposition parameters. Atomic ratios were calculated from the peak areas that were calibrated by the sensitive factors provided by the equipment manufacturer.

Au L_{III}-edge X-ray absorption spectroscopy (XAS) measurements of the catalyst samples were performed at the beam line 1W1B of Beijing Synchrotron Radiation Facility (BSRF), Institute of High Energy Physics (IHEP), Chinese Academy of Sciences (CAS). Au L_{III}-edge XAS spectra were collected at room temperature in the fluorescence mode using a solid state detector. The XAS spectra were analyzed with the program WinXAS 3.2 [36]. Background subtraction and normalization were performed by fitting linear polynomials to the pre-edge and the post-edge region of the absorption spectra, respectively. E_0 value was determined by the maximum in the first derivative in the edge region.

2.3. Catalyst tests and analytic procedures

Catalytic oxidation of CO was carried out in a quartz tubular flow microreactor with an internal diameter of 6.0 mm at atmospheric pressure, as described previously [35]. For each test, about 200 mg of catalyst sample (40–60 mesh) was placed at the center of the reactor using quartz glass wool as plugs. The catalyst was evaluated in the fresh state without any on-line pretreatment. The reaction stream consisted of 1.0 vol.% CO, 17.0 vol.% O_2 and balanced Ar; the weight hourly space velocity (WHSV) of the feed stream was 30 000 ml g^{-1} h^{-1}. After the reaction stream entered the reactor at room temperature, a light-off test (temperature-programmed reaction) was launched at a heating rate of 2 °C/min from room temperature to 200 °C or until CO was completely converted into CO_2. In the light-off profiles, the start temperature for a complete conversion of CO was used to evaluate the catalyst activity in CO oxidation.

CO and CO_2 in the effluent gas were periodically analyzed online with a gas chromatograph (Shimadzu GC-2010) equipped with a column packed with carbon molecular sieves, a post-column methanator that converted CO and CO_2 into CH_4, and a flame ionization detector (FID).

3. Results and discussions

3.1. Textural properties and XRD results

The BET surface areas and particle sizes of CeO_2–TiO_2 nanorods and nanoparticles as well as the corresponding supported gold catalysts were estimated by N_2 sorption, XRD and TEM measurements, as listed in Table 1. Both CeO_2–TiO_2-R and CeO_2–TiO_2-P are alike in the surface area; after loading the gold component, the surface areas of the resultant gold catalysts are also almost identical to those of the corresponding supports.

The compositions of Au/CeO_2–TiO_2 catalysts with different support morphologies determined by ICP analysis are listed in Table 2. It indicates that the molar ratios of CeO_2 to TiO_2 in both

Table 1
Textural properties of the CeO_2–TiO_2 supports and corresponding supported gold catalysts with different morphologies.

Samples	Surface area (m²/g)	Crystallite size[a] (nm)	Cell parameter[a] (nm)	Particle size[b] (nm)
CeO_2	–	–	0.5415	–
CeO_2–TiO_2-R	97.7	–	0.5387	–
Au/CeO_2–TiO_2-R	97.1	–	0.5377	10.5 × (40–200)
CeO_2–TiO_2-P	91.7	21.3	0.5391	–
Au/CeO_2–TiO_2-P	90.3	20.3	0.5397	10.9

[a] Average CeO_2 crystallite sizes were estimated from the broadening of CeO_2 (1 1 1), (2 0 0), (2 2 0), and (3 1 1) diffraction peaks by the Scherrer formula from XRD patterns and the cell parameters of cubic CeO_2 were obtained by the MDI Jade5 software.
[b] Particle sizes were estimated by measuring the sizes of randomly selected 300 typical particles in the TEM images of the catalyst samples.

Table 2
Compositios of the Au/CeO_2–TiO_2 catalysts with different support morphologies determined by ICP analysis.

Samples	Au content (wt.%)	Ti content (wt.%)	Ce content (wt.%)	CeO_2/TiO_2 molar ratio
Au/CeO_2–TiO_2-R	0.68	3.28	70.75	7.4
Au/CeO_2–TiO_2-P	0.94	3.38	69.84	7.1

Au/CeO_2–TiO_2-R and Au/CeO_2–TiO_2-P are close to the designated value of 8. The loading of gold on the Au/CeO_2–TiO_2-P catalyst (0.94 wt.%) is adjacent to the designated value (1 wt.%), while it is some lower on the Au/CeO_2–TiO_2-R catalyst (0.68 wt.%), which may suggest that the efficiency of gold deposition on CeO_2–TiO_2-R is somewhat lower than that on Au/CeO_2–TiO_2-P, though both supports are similar in the surface area (Table 1). This is probably attributed to the fact that the gold species is preferably deposited on the defect sites (e.g. vacancies, kinks, steps, etc.) of the support materials; the density of defect sites is related to their preparation method and the hydrothermal synthesis method is of benefit to give material surface free from defect. XRD patterns of the as-synthesized CeO_2–TiO_2 nanorods and nanoparticles as well as the corresponding supported gold catalysts are shown in Fig. 1. Compared with CeO_2–TiO_2-P, CeO_2–TiO_2-R shows stronger diffraction intensity, indicating a higher crystallinity and lower surface defect, which may then decrease the efficiency of gold deposition on CeO_2–TiO_2-R.

As shown in Fig. 1, both CeO_2–TiO_2-R and CeO_2–TiO_2-P show only face-centered cubic (fcc) fluorite structure of ceria. As the content of TiO_2 in these samples is relatively much lower (Table 2), titania phase is not detected in these XRD patterns; it is present
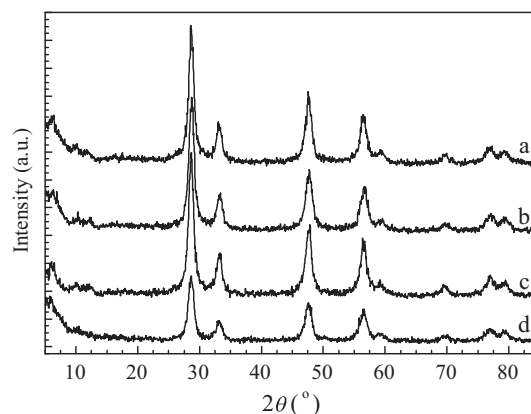

Fig. 1. XRD patterns of (a) CeO_2–TiO_2-R, (b) CeO_2–TiO_2-P, (c) Au/CeO_2–TiO_2-R, and (d) Au/CeO_2–TiO_2-P.

either as an amorphous phase or as small crystalline grains below the instrumental detection limit.

As listed in Table 1, the cell parameter of cubic CeO_2 in the CeO_2–TiO_2 composite is some smaller than that in pure CeO_2, similar to those reported for other ceria-related mixed oxides [28,35]. An interstitial solid solution may be formed through the entrance of a portion of Ti^{4+} ions into the lattice of CeO_2, because the radius of Ti^{4+} (0.068 nm) is smaller than those of Ce^{3+} (0.103 nm) and Ce^{4+} (0.099 nm). Due to the large difference between Ce^{3+}/Ce^{4+} and Ti^{4+} ions in their radius, according to the Hume-Rothery rules, the formation of Ce–Ti substitution solid solution is forbidden and the formation of interstitial one is more probable. However, Luo et al. found that the lattice parameter of the cubic phase in $Ce_xTi_{1−x}O_2$ was decreased with the decrease of x value from 1.0 to 0.6 [28]; they ascribed this phenomenon to the formation of a solid solution by substitution of Ce with Ti atoms in the CeO_2 lattice. In our previous work, the formation of CeO_2–TiO_2 solid solution was also reported, although we were uncertain whether it belongs to substitution or interstitial solid solution [37]. In addition, as stated above, the content of TiO_2 in the CeO_2–TiO_2 support is relatively lower and titania phase is not detected in the XRD patterns, and thence TiO_2 may also be present as an amorphous phase highly dispersed on the CeO_2 surfaces.

After the deposition of the gold component, the XRD patterns of the Au/CeO_2–TiO_2 catalysts remain unchanged compared with those of the corresponding CeO_2–TiO_2 supports, suggesting that the introduction of gold species does not induce any significant modification on the support phase; similar result was also observed by other researchers [27,38]. The average crystal sizes of CeO_2 in the

CeO_2–TiO_2-P support and the corresponding Au/CeO_2–TiO_2-P catalyst estimated from the diffraction lines of cerianite (1 1 1), (2 0 0), (2 2 0) and (3 1 1) planes are 21.3 and 20.3 nm, respectively. Moreover, there are also no diffraction peaks detected for Au species in any gold catalysts in this work, indicating that Au is finely dispersed on the supports with a particle size smaller than 5 nm.

3.2. TEM and HRTEM results

TEM and HRTEM images of Au/CeO_2–TiO_2-R and Au/CeO_2–TiO_2-P are shown in Fig. 2. It indicates again that the deposition of gold component does not alter the original morphology of the corresponding CeO_2–TiO_2 supports. Au/CeO_2–TiO_2-R is in the shape of rods with a uniform width of approximate 10 nm and a length of 40–200 nm (Fig. 2a, Table 1). Meanwhile, the Au/CeO_2–TiO_2-P catalyst has a particle diameter of around 10 nm (Fig. 2c, Table 1), which is somewhat different from that determined by XRD, possibly due to the non-spherical nature of Au/CeO_2–TiO_2-P particles.

The HRTEM images further illustrate that the exposed crystal planes of Au/CeO_2–TiO_2-R are dominated by (1 1 0) and (1 0 0) facets of CeO_2 (Fig. 2b), while Au/CeO_2–TiO_2-P mainly exposes (1 1 1) planes (Fig. 2d). TiO_2 crystallite planes are not observed in these two catalysts, though TiO_2 can be detected by ICP analysis (Table 2); this result supports that TiO_2 is present as very small particles or in amorphous phase [35] and a portion of Ti^{4+} ions is even incorporated into the lattice of CeO_2, consistent with the XRD results.

Notably, gold particles with a diameter smaller than 5 nm are identified on Au/CeO_2–TiO_2-R by the HRTEM images, while they
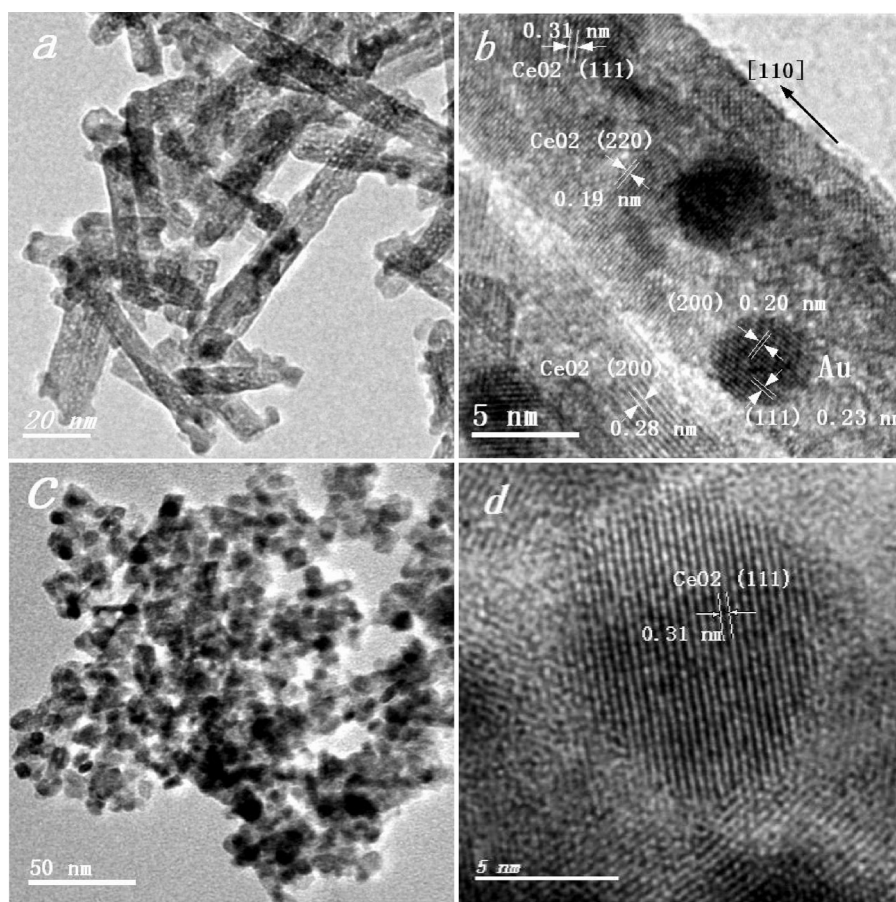

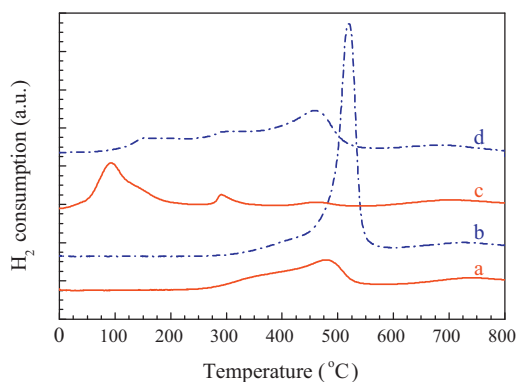**Fig. 2.** TEM and HRTEM images of (a) and (b) Au/CeO_2–TiO_2-R, and (c) and (d) Au/CeO_2–TiO_2-P.

Fig. 3. H_2-TPR profiles of (a) CeO_2–TiO_2-R, (b) CeO_2–TiO_2-P, (c) Au/CeO_2–TiO_2-R, and (d) Au/CeO_2–TiO_2-P.

are hardly observed on Au/CeO_2–TiO_2-P, possibly due to the low contrast of Au [39]. As suggested by Zhang et al. [40], ceria in the cubic fluorite structure owns three low-index planes, i.e. the very stable and neutral (1 1 1) plane, the less stable (1 1 0) plane, and the higher-energy (0 0 1) plane. CeO_2 nanorods with well-defined (0 0 1) and (1 1 0) reactive planes are more active than the "classical" CeO_2 nanoparticles with the neutral (1 1 1) planes in CO oxidation [41]. Therefore, the HRTEM results suggest that CeO_2–TiO_2-R obtained in this work are dominated by (1 1 0) and (1 0 0) facets, compared with CeO_2–TiO_2-P with (1 1 1) planes, which are beneficial to the dispersion of gold and in turn may contribute to the high catalytic activity of Au/CeO_2–TiO_2-R in CO oxidation.

3.3. H_2-TPR results

H_2-TPR has been extensively used to characterize the reducibility of oxygen species in CeO_2 and CeO_2 containing materials. Fig. 3 shows the H_2-TPR profiles of CeO_2–TiO_2 nanorods and nanoparticles along with the corresponding supported gold catalysts; the results of a quantitative analysis of the H_2-TPR profiles are listed in Table 3. As the content of TiO_2 in the CeO_2–TiO_2 supports is relatively low and TiO_2 is also much more difficult to reduce than CeO_2, the quantity of H_2 used here for the reduction of Ti species is then thought to be negligible in this work; therefore, the H_2 uptakes detected for CeO_2–TiO_2 supports are mainly ascribed to the reduction of CeO_2.

For CeO_2–TiO_2-R, the reduction of CeO_2 starts at 300 °C and a broad peak centered at 480 °C with a H_2 uptake of 910 μmol/g is observed, which is attributed to the reduction of the surface-capping oxygen of CeO_2, because bulk CeO_2 was generally reduced at a temperature above 800 °C [6,42]. Meanwhile, CeO_2–TiO_2-P shows an intense narrower peak for the surface-capping oxygen reduction at a slightly higher temperature (520 °C); the H_2 uptake for CeO_2–TiO_2-P reduction is much higher than that for CeO_2–TiO_2-R, indicating that CeO_2–TiO_2-P has much more surface oxygen than

CeO_2–TiO_2-R (Table 3). The TEM images shown in Fig. 2 suggest that CeO_2–TiO_2-P has a smaller particle size, which may also give it more surface oxygen than CeO_2–TiO_2-R. As suggested by Zhou et al. [41], the quantity of H_2 consumed for the reduction of CeO_2 was related to the amount of amorphous ceria clusters in the fresh nanoparticles; these fine ceria clusters were very sensitive to the reducing atmosphere.

The reducibility of the gold catalysts is changed greatly after loading the gold component, compared with that of the corresponding CeO_2–TiO_2 supports (Fig. 3). The reduction peaks of the surface ceria shift from 480 °C to 460 °C and from 520 °C to 460 °C for Au/CeO_2–TiO_2-R and Au/CeO_2–TiO_2-P, respectively. Moreover, two noticeable new peaks appear at lower temperatures for both gold catalysts. One presents itself at about 290 °C, which can be assigned to the reduction of the surface-capping oxygen of CeO_2; another appears at very low temperatures (around 90 °C for Au/CeO_2–TiO_2-R and 150 °C for Au/CeO_2–TiO_2-P), which should be assigned to the reduction of CeO_2 strongly bound with the gold species [15]. These low temperature peaks for the reduction of CeO_2 overlapped with those for the reduction of cationic gold species, if their presence was assumed [43]. Noticeably, the Au/CeO_2–TiO_2-R catalyst exhibits much intenser low temperature reduction peak than Au/CeO_2–TiO_2-P (Fig. 3 and Table 3), illustrating that the former owns a much higher fraction of strongly bound surface gold species; moreover, the intensity of low temperature reduction peak for Au/CeO_2–TiO_2-R becomes even higher than that of the high temperature reduction peak.

These results clearly demonstrate that the incorporation of gold in CeO_2–TiO_2 promotes the reduction of CeO_2, especially for Au/CeO_2–TiO_2 nanorods. The reduction of ceria-related materials was strongly facilitated by the presence of Au [23,43] and Pd [6], which may be attributed to the spillover phenomena involving either hydrogen activated on the metal phase or lattice CeO_2 oxygen induced by intimate metal-support interactions. In addition, as reported by Mai et al. [44], the migration of lattice oxygen from bulk to surface on the (1 1 0)/(1 0 0) facet-dominated catalyst is much easier compared with that on the (1 1 1) facet-dominated one, which may also significantly contribute to the strong redox capacity of Au/CeO_2–TiO_2-R.

In summary, the low-temperature peaks in the H_2-TPR profiles of Au/CeO_2–TiO_2 are attributed to the reduction of the surface oxygen species of CeO_2 strongly bound with the gold species, which are catalytically active for CO oxidation [41,45]; as a result, compared with Au/CeO_2–TiO_2-P, the Au/CeO_2–TiO_2-R catalyst with higher redox ability may also imply a higher catalytic activity.

3.4. XPS results

XPS measurements were performed to determine the surface composition and oxidation state of the gold catalysts of different morphologies. As shown in Fig. 4, Au/CeO_2–TiO_2-R and Au/CeO_2–TiO_2-P are similar in their Au 4f XPS spectra; both catalysts exhibit a pair of distinct peaks at around 83.7 and 87.5 eV, which are the characteristics of metallic Au [46,47]. The peaks located around 85.5 and 86.3 eV for the oxidized Au species cannot be detected [48], similar to that observed for Au/TiO_2 catalyst prepared by the same colloidal deposition method [12]. It was known that the gold species in the catalyst prepared by deposition–precipitation and co-precipitation methods can be in the forms of metallic Au, Au_2O_3, Au (OH)$_3$ and AuOOH·$n$$H_2O$; the performances of gold catalyst may be determined jointly by a mixture of these species with various nanostructures [16]. However, by using the colloidal deposition method, the colloidal gold metal particles are generated before they are deposited on the support and the formation of the gold particles is then well controlled; as a result, the effect of the support on the catalytic activity may

Table 3
Quantitative analysis of the H_2-TPR profiles of the gold catalysts and corresponding CeO_2–TiO_2 supports with different morphologies.

Samples	Peak position (°C)	H_2 uptake (μmol/g)	Theoretical H_2 uptake (μmol/g)[a]
CeO_2–TiO_2-R	480	910	2055
Au/CeO_2–TiO_2-R	92, 292, 460	661, 196, 137	2055
CeO_2–TiO_2-P	520	1690	2029
Au/CeO_2–TiO_2-P	150, 297, 460	181, 432, 890	2029

[a] Theoretical H_2 uptake was determined as the quantity of H_2 required for the reduction of Au catalysts and corresponding CeO_2–TiO_2 supports by assuming that CeO_2 is stoichiometrically reduced to Ce_2O_3.

Table 4
XPS results of the gold catalysts and corresponding CeO_2–TiO_2 supports with different morphologies.

Samples	Au content (at.%)		Au $4f_{7/2}$ BE (eV)	Ce^{3+} content (at.%)	Au/(Ce + Ti) atomic ratio	O/(Ce + Ti) atomic ratio
	ICP	XPS				
CeO_2–TiO_2-R	–	–	–	24.03	–	2.35
CeO_2–TiO_2-P	–	–	–	20.17	–	2.45
Au/CeO_2–TiO_2-R	0.16	2.86	83.7, 87.5	24.11	0.11	2.76
Au/CeO_2–TiO_2-P	0.22	1.74	83.8, 87.5	20.41	0.06	2.34

be properly isolated from a variety of other factors. Therefore, as the gold nanoparticles are deposited on the CeO_2–TiO_2 supports of different morphologies by the colloidal deposition method in the present study, the influence of gold species on the catalytic behavior can be excluded to get a deep insight into the effect of the support morphology on the performance of Au/CeO_2–TiO_2 catalysts [12]. In addition, the metallic gold species could activate the hydrogen with subsequent spillover on the support and promote the reduction of ceria at low temperature [47], which is in good agreement with the H_2-TPR results.

The bulk and surface gold compositions determined by ICP-AES and XPS, respectively, are listed in Table 4. Au/CeO_2–TiO_2-R has a bulk gold composition of 0.16 at.% (0.68 wt.%), which is a little lower than the value of 0.22 at.% (0.94 wt.%) for Au/CeO_2–TiO_2-P. The bulk gold content is close to the expected value; however, the surface gold content is much higher than the bulk gold content for both catalysts, which means that the gold species is enriched on the support surface. Moreover, it is noteworthy that the surface gold content in Au/CeO_2–TiO_2-R (2.86 at.%) is much higher than that in Au/CeO_2–TiO_2-P (1.74 at.%), just opposite to the order for bulk gold content. As suggested by Sayle et al. [49], the formation of anion vacancies is easier on CeO_2 surfaces of (1 1 0) planes than that on (1 0 0) and (1 1 1) planes, according to their formation energies. Therefore, the CeO_2–TiO_2-R support dominated with (1 1 0) and (1 0 0) planes should perform better in anchoring and dispersing gold particles than CeO_2–TiO_2-P dominant with (1 1 1) facets [15], which endues the Au/CeO_2–TiO_2-R catalyst with high gold dispersion and surface content.

Fig. 5 shows the XPS spectra of Ce 3d region of the supports and Au-containing catalysts; two types of cerium oxides are present, i.e. Ce(III) and Ce(IV). The appearance of high U′′′ and V′′′ signals (916.5 and 898.4 eV), together with U and V peaks (901.3 and 882.7 eV) which are less intense than the U′′ and V′′ peaks (907.7 and 888.9 eV), is an evidence of the presence of Ce(IV). The appearance of U′, V′, U^0, and V^0 signals located at about 903.5, 884.6, 899.0, and 880.6 eV, respectively, indicates the existence of Ce(III) states [50], which is attributed to the interaction between ceria and the surrounding atoms and may also be used as an indicator for the

existence of oxygen vacancies. The contents of Ce(III) ($C_{Ce(III)}$) listed in Table 4 are evaluated from the peak area of Ce 3d core lever according to the following equations:

$$A_{Ce(III)} = U^0 + V^0 + U' + V'$$

$$A_{Ce(IV)} = U + V + U'' + V'' + U''' + V'''$$

$$C_{Ce(III)} = A_{Ce(III)}/[A_{Ce(III)} + A_{Ce(IV)}]$$

It is noteworthy again that the contents of Ce(III) in CeO_2–TiO_2-R (24.03%) and in Au/CeO_2–TiO_2-R (24.17%) are also much higher than those in CeO_2–TiO_2-P (20.17%) and in Au/CeO_2–TiO_2-P (20.41%). This further indicates that the oxygen vacancies are easier to form on the CeO_2–TiO_2-R support surface dominated with (1 1 0) and (1 0 0) facets than that on the CeO_2–TiO_2-P with (1 1 1) planes; the higher density of oxygen vacancies in CeO_2–TiO_2-R is of benefit to get a higher Au dispersion and activity of the Au/CeO_2–TiO_2-R catalyst in CO oxidation [51,52].

The O 1s spectra of CeO_2–TiO_2 supports and Au-containing catalysts are depicted in Fig. 6. The main peak detected at 529.1–529.5 eV is related to the lattice oxygen of cerium oxide and titanic oxide; the distinct shoulders with higher binding energy (532.1 eV) are attributed to hydroxide and adsorbed water on the catalyst surface [51]. Au/CeO_2–TiO_2-R exhibits a stronger intensity for this shoulder at higher binding energy than Au/CeO_2–TiO_2-P, indicating a greater tendency to form hydroxide or hydroxyl on the surface of the Au/CeO_2–TiO_2-R catalyst. Table 4 further displays that the atomic ratio of the total surface oxygen (O_T) to the Ce + Ti atoms is higher than the corresponding stoichiometric values in the CeO_2–TiO_2 supports and the Au-containing catalysts. These suggest the presence of large amount of oxygen-containing
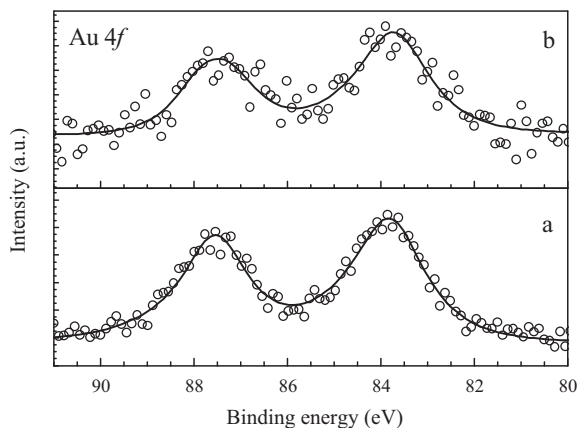
Fig. 4. Au 4f XPS spectra of (a) Au/CeO_2–TiO_2-P and (b) Au/CeO_2–TiO_2-R.
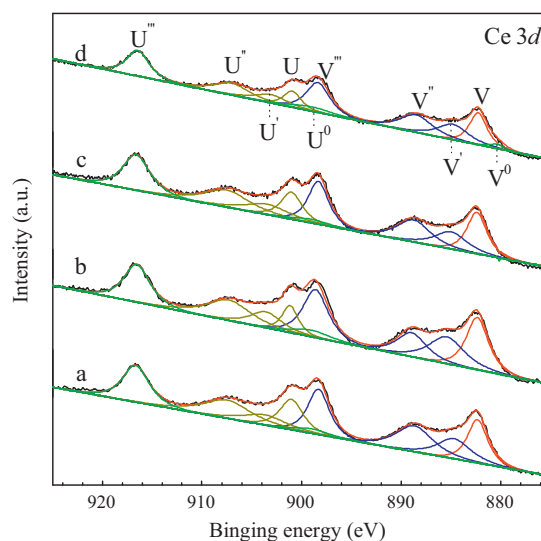
Fig. 5. Ce 3d XPS spectra of (a) CeO_2–TiO_2-P, (b) CeO_2–TiO_2-R, (c) Au/CeO_2–TiO_2-P, and (d) Au/CeO_2–TiO_2-R.
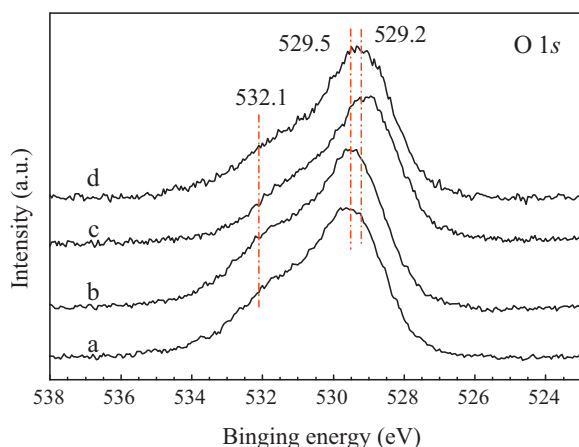
Fig. 6. O 1s XPS spectra of (a) CeO_2–TiO_2-P, (b) CeO_2–TiO_2-R, (c) Au/CeO_2–TiO_2-P, and (d) Au/CeO_2–TiO_2-R.

species in CeO_2–TiO_2 supports and Au-containing catalysts (especially in the Au/CeO_2–TiO_2-R catalyst, where a pronouncedly high surface O_T/(Ce + Ti) ratio is identified); similar observations were also reported for the Au/MnO_2 (rod) catalyst [48].

3.5. XAS results

Fig. 7 shows the Au L_{III}-edge X-ray absorption near-edge structure (XANES) spectra of the Au/CeO_2–TiO_2-P and Au/CeO_2–TiO_2-R catalysts, together with Au foil as a reference. Gold foil (Au⁰) shows a shoulder at 11 933 eV as well as two intense peaks at 11 947 and 11 970 eV; the peaks at 11 933 and 11 947 eV are characteristic for pure gold fcc structure ordered up to the third shell [53]. Fig. 7 clearly illustrates that both Au/CeO_2–TiO_2-R and Au/CeO_2–TiO_2-P are identical to Au foil in their Au L_{III}-edge XANES spectra. Since XAS is a very sensitive technique in detecting Au cations, which gives a strong peak at 11 921.6 eV in the Au L_{III}-edge XANES spectrum [54], the absence of this peak in the spectra of Au/CeO_2–TiO_2-R and Au/CeO_2–TiO_2-P further confirms the absence of Au cations in these catalysts, in well agreement with the XPS results.

3.6. Catalytic performance of Au/CeO_2–TiO_2 in CO oxidation

3.6.1. Effect of the support morphology on the catalyst performance

The effects of support morphology on the performances of the Au/CeO_2–TiO_2 catalysts (as well as the parent CeO_2–TiO_2 supports) in CO oxidation were considered, as shown in Fig. 8. Both
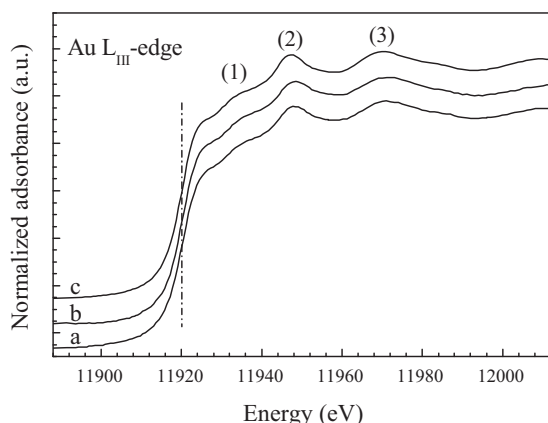

Fig. 7. XANES spectra of (a) Au/CeO_2–TiO_2-P, (b) Au/CeO_2–TiO_2-R, and (c) Au foil.
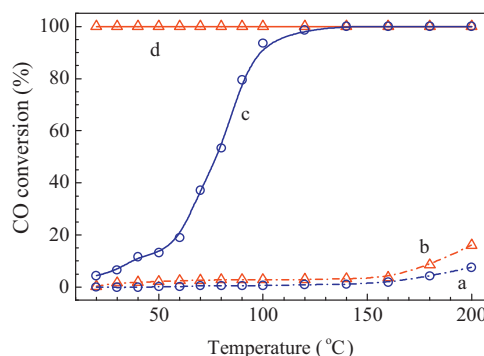
Fig. 8. Catalytic activities determined by the light-off tests in CO oxidation of (a) CeO_2–TiO_2-P, (b) CeO_2–TiO_2-R, (c) Au/CeO_2–TiO_2-P, and (d) Au/CeO_2–TiO_2-R.

CeO_2–TiO_2-R and CeO_2–TiO_2-P exhibit poor activity in CO oxidation, though the former (CeO_2–TiO_2-R) is slightly more active. After loading Au, the activity of the supported gold catalysts is evidently enhanced, confirming the essential role of gold in CO oxidation. Moreover, Fig. 8 also clearly displays a significant effect of support morphology on the catalyst performance; the Au/CeO_2–TiO_2-R catalyst exhibits a markedly higher activity than Au/CeO_2–TiO_2-P. Over the Au/CeO_2–TiO_2-R catalyst, CO can be completely converted to CO_2 even at ambient temperature (20 °C), whereas the complete conversion of CO is achieved at 120 °C over the Au/CeO_2–TiO_2-P catalyst.

3.6.2. Activation of Au/CeO_2–TiO_2 catalysts

As reported by Schüth and coworkers, a thermal activation is necessary for the uncalcined Au/TiO_2 catalysts prepared by the colloidal deposition method before the catalytic activity test, probably due to the inhibitory effect of the residual protecting agent (PVA) on the catalyst activity [12]. In the present work, the effect of the calcination temperature on the catalytic performance of Au/CeO_2–TiO_2 was also considered. As shown in Fig. 9, both the uncalcined Au/CeO_2–TiO_2-R and Au/CeO_2–TiO_2-P catalysts exhibit poor activity in CO oxidation at low temperature for the very first
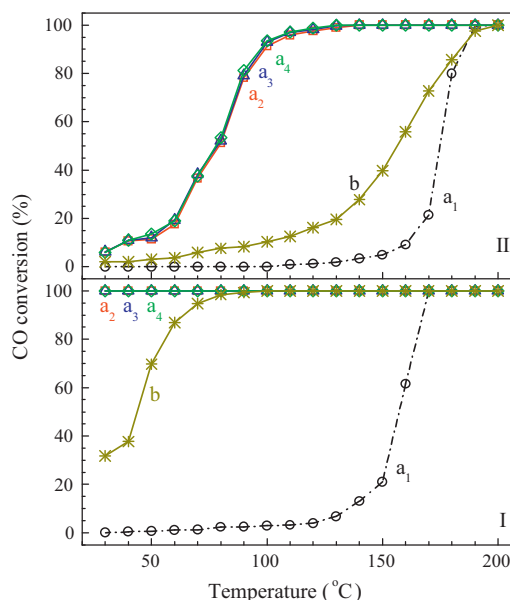

Fig. 9. Effect of calcination and activation on the catalytic activities in CO oxidation of (I) Au/CeO_2–TiO_2-R and (II) Au/CeO_2–TiO_2-P. Lines of (a_1), (a_2), (a_3) and (a_4) are the successive light-off test profiles of the uncalcined catalyst samples, for the 1st, 2nd, 3rd and 4th runs, respectively; line (b) is the light-off test profile of the catalyst samples calcined at 450 °C in air for 4 h.
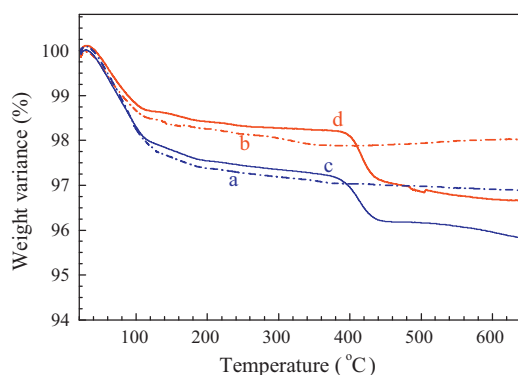
Fig. 10. TG analysis of (a) CeO$_2$–TiO$_2$-R, (b) CeO$_2$–TiO$_2$-P, (c) Au/CeO$_2$–TiO$_2$-R, and (d) Au/CeO$_2$–TiO$_2$-P.

run test; the complete conversion of CO is only achieved at 170 and 190 °C over the Au/CeO$_2$–TiO$_2$-R and Au/CeO$_2$–TiO$_2$-P catalysts, respectively. However, the catalysts are obviously activated by the first run test; the light-off profiles for the subsequent tests significantly shift to lower temperatures compared with the first run test of the very fresh uncalcined catalysts. After the activation by the first run light-off test, CO can be completely converted to CO$_2$ at ambient temperature (20 °C) over Au/CeO$_2$–TiO$_2$-R and at 120 °C over Au/CeO$_2$–TiO$_2$-P, the same as those obtained on the catalysts calcined in air at 250 °C for 4 h (Fig. 8). Current results confirm the necessity of the thermal activation process for the Au/TiO$_2$ catalysts prepared by the colloidal deposition, which is in good agreement with the report of Schüth and coworkers [12].

As a protective agent (PVA) was used during the preparation of the gold catalysts, TG analysis was performed to examine whether the organic species (PVA) was completely removed by later calcination pretreatment at 250 °C. As shown in Fig. 10, the weight loss around 100 °C and that at 370–440 °C are ascribed to the removals of adsorbed water and organic species, respectively; the later accounts for about 1% of the total catalyst weight. Such a result suggests that the organic protective agent cannot be completely removed through the calcination at 250 °C; it requires a temperature of about 450 °C.

The gold catalysts were then calcined in air at 450 °C for 4 h to remove the organic species completely and their performances in CO oxidation are also shown in Fig. 9. Obviously, the activity of the gold catalysts calcined at 450 °C is decreased substantially, compared with that of the uncalcined catalysts after the first run and those calcined at 250 °C (Fig. 8), which may be ascribed to the fact that the gold particles are susceptible to aggregation upon the thermal treatment at high temperature. It can be deduced that the residual protecting agent or the stabilizer in the catalysts calcined at low temperature (200–250 °C) may play an important role in the isolation of the gold particles, which is effective in suppressing the sintering of gold nanoparticles. Accordingly, the thermal treatment at 250 °C is preferred for the activation of Au/CeO$_2$–TiO$_2$ catalysts, though the stabilizers may not be completely removed at this temperature. Moreover, all the light-off tests after the activation by the first run test are almost identical in their light-off profiles (Fig. 9), suggesting that the activity of the Au/CeO$_2$–TiO$_2$ catalyst is quite stable during these test cycles.

It was reported that the Au nanoparticles prepared by colloidal deposition method essentially maintain their metallic state and particle size distribution on different supports [12]. In current work, both the Au/CeO$_2$–TiO$_2$-R and Au/CeO$_2$–TiO$_2$-P catalysts are identical in the colloidal deposition conditions for loading gold particles; the N$_2$ sorption, XPS and XAS results also demonstrate that these two catalysts are alike in the surface area and the state of Au nanoparticles. Therefore, the difference between the

Au/CeO$_2$–TiO$_2$-R and Au/CeO$_2$–TiO$_2$-P catalysts in the performance of CO oxidation should be ascribed to their difference in the nature of the support, i.e. the morphology of CeO$_2$–TiO$_2$. CeO$_2$–TiO$_2$-R exposes mainly (1 1 0) and (1 0 0) facets, which should be beneficial to the oxygen migration and gold dispersion. As a result, the Au/CeO$_2$–TiO$_2$-R catalyst is provided with a much higher fraction of strongly bound gold species on the surface as well as excellent redox ability, compared with the Au/CeO$_2$–TiO$_2$-P catalyst. All these may contribute to the high activity of Au/CeO$_2$–TiO$_2$-R in CO oxidation at low temperature.

4. Conclusions

Au/CeO$_2$–TiO$_2$ catalysts with different support morphologies (nanorods and nanoparticles) were prepared by the colloidal deposition method and used in CO oxidation at low temperature. HRTEM results show that Au/CeO$_2$–TiO$_2$-R is dominated by (1 1 0) and (1 0 0) facets of CeO$_2$, while the Au/CeO$_2$–TiO$_2$-P mainly expose (1 1 1) planes. The N$_2$ sorption, XPS and XAS results demonstrate that both Au/CeO$_2$–TiO$_2$-R and Au/CeO$_2$–TiO$_2$-P are alike in the surface area and the state of Au nanoparticles. H$_2$-TPR results indicate that the presence of Au strongly promotes the reduction of CeO$_2$ in the Au/CeO$_2$–TiO$_2$-R catalyst.

The catalytic activity of Au/CeO$_2$–TiO$_2$ in CO oxidation is strongly related to the morphology of CeO$_2$–TiO$_2$; CeO$_2$–TiO$_2$-R as support gives the Au/CeO$_2$–TiO$_2$-R catalyst much higher activity than CeO$_2$–TiO$_2$-P to Au/CeO$_2$–TiO$_2$-P. The (1 1 0) and (1 0 0) CeO$_2$ facets dominated in the Au/CeO$_2$–TiO$_2$-R catalyst are able to promote the oxygen migration and gold dispersion; as a result, the Au/CeO$_2$–TiO$_2$-R catalyst is provided with a much higher fraction of strongly bound gold species on the surface as well as excellent redox ability, compared with the Au/CeO$_2$–TiO$_2$-P catalyst. All these may contribute to the high activity of Au/CeO$_2$–TiO$_2$-R in CO oxidation at low temperature.

References

[1] M. Haruta, N. Yamada, T. Kobayashi, S. Iijima, J. Catal. 115 (1989) 301.
[2] M. Haruta, S. Tsubota, T. Kobayashi, H. Kageyama, M.J. Genet, B. Delmon, J. Catal. 144 (1993) 175.
[3] W.C. Li, M. Comotti, F. Schüth, J. Catal. 237 (2006) 190.
[4] E. Smolentseva, A. Simakov, S. Beloshapkin, M. Estrada, E. Vargas, V. Sobolev, R. Kenzhin, S. Fuentes, Appl. Catal. B 115 (2012) 117.
[5] J.N. Lin, J.H. Chen, C.Y. Hsiao, Y.M. Kang, B.Z. Wan, Appl. Catal. B 36 (2002) 19.
[6] H.Q. Zhu, Z.F. Qin, W.J. Shan, W.J. Shen, J.G. Wang, J. Catal. 225 (2004) 267.
[7] L.Q. Liu, F. Zhou, L.G. Wang, X.J. Qi, F. Shi, Y.Q. Deng, J. Catal. 274 (2010) 1.
[8] S.E. Golunski, H.A. Hatcher, R.R. Rajaram, T.J. Truex, Appl. Catal. B 5 (1995) 367.
[9] Y.J. Mergler, A. van Aalst, J. van Delft, B.E. Nieuwenhuys, Appl. Catal. B 10 (1996) 245.
[10] M. Haneda, T. Watanabe, N. Kamiuchi, M. Ozawa, Appl. Catal. B 142 (2013) 14.
[11] M. Haruta, Catal. Today 36 (1997) 153.
[12] M. Comotti, W.C. Li, B. Spliethoff, F. Schüth, J. Am. Chem. Soc. 128 (2006) 917.
[13] M.M. Schubert, V. Plzak, J. Garche, R.J. Behm, Catal. Lett. 76 (2001) 143.
[14] M.M. Schubert, S. Hackenberg, A.C. van Veen, M. Muhler, V. Plzak, R.J. Behm, J. Catal. 197 (2001) 113.
[15] R. Si, M. Flytzani-Stephanopoulos, Angew. Chem. Int. Ed. 47 (2008) 2884.
[16] G.H. Wang, W.C. Li, K.M. Jia, B. Spliethoff, F. Schüth, A.H. Lu, Appl. Catal. A 364 (2009) 42.
[17] Z. Zhong, J. Ho, J. Teo, S. Shen, A. Gedanken, Chem. Mater. 19 (2007) 4776.
[18] Y.F. Han, Z. Zhong, K. Ramesh, F. Chen, L. Chen, J. Phys. Chem. C 111 (2007) 3163.
[19] Q. Fu, W. Deng, H. Saltsburg, M. Flytzani-Stephanopoulos, Appl. Catal. B 56 (2005) 57.
[20] W.J. Cai, F.G. Wang, A.C. van Veen, H. Provendier, C. Mirodatos, W.J. Shen, Catal. Today 138 (2008) 152.

[21] J. Kašpar, P. Fornasiero, M. Graziani, Catal. Today 50 (1999) 285.
[22] A. Trovarelli, Catal. Rev. Sci. Eng. 38 (1996) 439.
[23] L. Ilieva, G. Pantaleo, I. Ivanov, A. Maximova, R. Zanella, Z. Kaszkur, A.M. Venezia, D. Andreeva, Catal. Today 158 (2010) 44.
[24] L. Ilieva, G. Pantaleo, J.W. Sobczak, I. Ivanov, A.M. Venezia, D. Andreeva, Appl. Catal. B 76 (2007) 107.
[25] P. Haider, J.D. Grunwaldt, R. Seidel, A. Baiker, J. Catal. 250 (2007) 313.
[26] I. Dobrosz-Gómez, I. Kocemba, J.M. Rynkowski, Appl. Catal. B 83 (2008) 240.
[27] H. Wang, H.Q. Zhu, Z.F. Qin, G.F. Wang, F.X. Liang, J.G. Wang, Catal. Commun. 9 (2008) 1487.
[28] M.F. Luo, J. Chen, L.S. Chen, J.Q. Lu, Z.C. Feng, C. Li, Chem. Mater. 13 (2001) 197.
[29] C. Gennequin, M. Lamallem, R. Cousin, S. Siffert, F. Aïssi, A. Aboukaïs, Catal. Today 122 (2007) 301.
[30] Y. Zhang, Z.X. Li, X.B. Wen, Y. Liu, Chem. Eng. J. 121 (2006) 115.
[31] J.L. Ye, Y.Q. Wang, Y. Liu, H. Wang, Int. J. Hydrogen Energy 33 (2008) 6602.
[32] G.L. Dong, J.G. Wang, Y.B. Gao, S.Y. Chen, Catal. Lett. 58 (1999) 37.
[33] H.Q. Zhu, Z.F. Qin, W.J. Shan, W.J. Shen, J.G. Wang, J. Catal. 233 (2005) 41.
[34] F.X. Liang, H.Q. Zhu, Z.F. Qin, H. Wang, G.F. Wang, J.G. Wang, Catal. Lett. 126 (2008) 353.
[35] Z.W. Wu, H.Q. Zhu, Z.F. Qin, H. Wang, L.C. Huang, J.G. Wang, Appl. Catal. B 98 (2010) 204.
[36] T. Ressler, J. Wong, J. Roos, I.L. Smith, Environ. Sci. Technol. 34 (2000) 950.
[37] H.Q. Zhu, Z.F. Qin, J.G. Wang, Chin. J. Catal. 26 (2005) 377.
[38] P. Sangeetha, Y.W. Chen, Int. J. Hydrogen Energy 34 (2009) 7342.
[39] G. Yi, H.W. Yang, B.D. Li, H.Q. Lin, K. Tanaka, Y.Z. Yuan, Catal. Today 157 (2010) 83.
[40] F. Zhang, Q. Jin, S.W. Chan, J. Appl. Phys. 95 (2004) 4319.
[41] K.B. Zhou, X. Wang, X.M. Sun, Q. Peng, Y.D. Li, J. Catal. 229 (2005) 206.
[42] D. Terribile, A. Trovarelli, C. de Leitenburg, G. Dolcetti, Chem. Mater. 9 (1997) 2676.
[43] O.H. Laguna, F. Romero Sarria, M.A. Centeno, J.A. Odriozola, J. Catal. 276 (2010) 360.
[44] H.X. Mai, L.D. Sun, Y.W. Zhang, R. Si, W. Feng, H.P. Zhang, H.C. Liu, C.H. Yan, J. Phys. Chem. B 109 (2005) 24380.
[45] H.C. Yao, Y.F. Yu Yao, J. Catal. 86 (1984) 254.
[46] L. Fan, N. Ichikuni, S. Shimazu, T. Uematsu, Appl. Catal. A 246 (2003) 87.
[47] X.S. Huang, H. Sun, L.C. Wang, Y.M. Liu, K.N. Fan, Y. Cao, Appl. Catal. B 90 (2009) 224.
[48] L.C. Wang, Y.M. Liu, M. Chen, Y. Cao, H.Y. He, K.N. Fan, J. Phys. Chem. C 112 (2008) 6981.
[49] T.X.T. Sayle, S.C. Parker, D.C. Sayle, Phys. Chem. Chem. Phys. 7 (2005) 2936.
[50] E. Bêche, P. Charvin, D. Perarnau, S. Abanades, G. Flamant, Surf. Interface Anal. 40 (2008) 264.
[51] J. Światowska, V. Lair, C. Pereira-Nabais, G. Cote, P. Marcus, A. Chagnes, Appl. Surf. Sci. 257 (2011) 9110.
[52] R. Leppelt, B. Schumacher, V. Plzak, M. Kinne, R.J. Behm, J. Catal. 244 (2006) 137.
[53] M.P. Casaletto, A. Longo, A.M. Venezia, A. Martorana, A. Prestianni, Appl. Catal. A 302 (2006) 309.
[54] K. Qian, H.X. Sun, W.X. Huang, J. Fang, S.S. Lv, B. He, Z.Q. Jiang, S.Q. Wei, Chem. Eur. J. 14 (2008) 10595.